

ARTICLE OPEN



Corrosion performance of wire arc additively manufactured NAB alloy

Ayda Shahriari¹✉, Dharmendra Chalasani¹, Babak Shalchi Amirkhiz^{1,2} and Mohsen Mohammadi¹

Nickel–aluminum bronzes (NAB) are vital alloys, known for biofouling resistance, crucial for marine and shipbuilding industries. This study examined corrosion performance of NAB samples fabricated by wire arc additive manufacturing (WAAM) in as-built and heat-treated conditions. Microstructural analysis revealed the WAAM-NAB parts primarily consisted of the α -phase (copper) and three types of κ -phases: κ_{II} (spherical Fe_3Al), κ_{III} (Ni–Al in lamellar shape) within the interdendritic areas, and iron-rich κ_{IV} particles dispersed throughout the matrix. In contrast, casting-produced NAB showed the formation of a rosette-like κ_I phase as well. Corrosion behavior comparisons between the two NAB fabrication methods were also assessed. The microstructural characterizations revealed a rise in the size of the κ_{IV} particles after heat-treated at 350 °C for 2 h (HT₁). Heat treatment at 550 °C for 4 h (HT₂) resulted in a needle-like κ_V , coarsening of κ_{II} , partial spheroidization of κ_{III} , and reduced κ_{IV} precipitation. When heat-treated to 675 °C for 6 h (HT₃), κ_{II} and κ_V were coarsened, κ_{III} was completely spheroidized, and κ_{IV} precipitation was significantly reduced. These microstructural features in HT₂ and HT₃ conditions steeply decreased their corrosion resistance compared to the WAAM as-built part. The as-built WAAM sample showed superior corrosion resistance in chloride solution, attributed to fewer κ -intermetallic phases and a finer microstructure. The κ -phases, irrespective of morphology, act as the cathodic areas versus the α -dendritic matrix, fostering microgalvanic cell formation. Consequently, precipitation of all cathodic κ -phases draws a higher galvanic current of the anodic α -phase, meaning a lower corrosion resistance.

npj Materials Degradation (2023)7:85; <https://doi.org/10.1038/s41529-023-00405-x>

INTRODUCTION

Cu–Al–Ni–Fe alloys containing 6–13 wt.% Al, and up to 7 wt.% Fe and Ni are known as nickel–aluminum bronze (NAB). The weight percent of Fe and Ni is about 3–6% in the more common copper alloys. In addition, Mn is added to these alloys up to ~1.5% to act as a deoxidant and a strengthening element¹. Their high resistance to corrosion and favorable tribological characteristics, including high resistance to erosion, wear, and cavitation in marine environments, make them proper candidates for manufacturing valves, turbines, and propellers^{2,3}. NAB alloys could have a revolutionary role in the maritime sectors by merging two critical attributes—corrosion resistance and biofouling mitigation. As ships traverse the expansive oceans and endure the corrosive effects of saltwater, and as marine organisms seek to find a foothold on vessel surfaces, NAB alloys have emerged as a good solution. Therefore, these alloys could shield marine structures from the clutches of corrosion and act as an unwavering defense against the relentless attachment of biofouling organisms. The symbiotic interplay of these qualities enhances the efficiency and longevity of marine assets via increasing sustainability and reducing the need for toxic anti-fouling treatments^{4–6}.

The microstructure of NAB alloys has a close relationship with the solidification rate. The complex phase transformation occurs during the casting process. Commonly, in as-cast alloys of NAB, the matrix consists of the solid solution rich in copper (referred to as the α -phase), along with preserved β -phase and intermetallic κ -precipitates. The κ -precipitates appear in the interdendritic areas and the matrix during the cooling and are numbered based on the order in which they precipitate in the microstructure as the temperature decreases. Accordingly, the large precipitate with a rosette morphology is κ_I , the smaller spheroidic precipitate at the

interdendritic region with dimensions of 5–10 μm is κ_{II} , and the lathe-shaped lamellar intermetallic phase is κ_{III} , and the κ_{IV} has finely distributed with a diameter lower than 1 μm in α -matrix^{1,7}.

The industry's contemporary needs entail crafting intricate structures with reduced material waste, porosity levels, production duration, and expenses. Simultaneously, there's a push for heightened deposition rates, energy efficiency, density, and precision in shape. These requirements have spurred the adoption of innovative manufacturing techniques, particularly the wire arc additive manufacturing (WAAM) method⁸. Within the WAAM procedure, a wire serves as the input material, undergoing fusion and placement onto a substrate. Three widely used WAAM processes are based on plasma arc welding, gas metal arc welding (GMAW), as well as gas tungsten arc welding. Among these three WAAM methods, GMAW has the maximum energy efficiency and is more adaptable than other AM methods known for their swift deposition rates, low production time, and material utilization⁹.

GMAW-WAAM has found many applications in the fabrication of the propeller of Al–Mg alloys⁹, injection molds of stainless steels¹⁰, and aerospace components from the Ti–6Al–4V alloy¹¹. This technique is also used in repairing applications to surface defects¹² and joining processes of the aluminum components to the carbon fiber reinforced polymers¹³. The fabrication of the NAB-C95800 using GMAW-WAAM is currently more demanding in the marine and shipbuilding industries. WAAM effectively reduces the manufacturing costs of metal components. It achieves this by minimizing the requirement for extensive stock storage, ease of powder management, and reducing waste material generation^{8,14}.

The combination of the input process parameters, cooling strategy, and post-treatments convey a different microstructural feature developed in a WAAM component compared to its

¹Marine Additive Manufacturing Centre of Excellence, University of New Brunswick, Fredericton, NB E3B 5A1, Canada. ²CanmetMATERIALS, Natural Resources Canada, 183 Longwood Road South, Hamilton, ON, Canada. ✉email: ashahria@unb.ca

counterpart produced using casting techniques. Since there is a close correlation between the microstructural attributes and the corrosion response of a metal part within a given environment, the corrosion behavior of the GMAW-WAAM-NAB component could be completely different than its as-cast counterpart. It is well-known κ -phases precipitated in the α -matrix of a NAB alloy show different preferences to the corrosion attacks in the chloride media^{15–18}.

Cuplan¹⁵ and Al-Hashem¹⁶ have found that the κ_1 and κ_{II} remained intact while the α and retained- β phases adjacent to the lamellar κ_{III} is corroded in a seawater solution. Moreover, the affinity to oxidation reactions is higher for the α -phase in comparison Fe–Ni–Al-abundant κ_1 , κ_{II} , and κ_{III} phases¹⁸. Song et al.¹⁹ investigated the nobility of the κ -phases in two different media, including acidic and neutral pH chloride solutions. Their results showed the κ -phases remained safeguarded within a chloride solution of neutral pH while corroded in an acidic environment.

Additive manufacturing in general and particularly WAAM have brought about a transformative shift in the fabrication of metallic alloys, especially in the context of strategic marine sectors, where NAB alloys hold a significant importance. Notably, the susceptibility to biofouling and corrosion remains a critical concern in assessing the practicality of marine alloys. In this context, the interrelationship between biofouling and corrosion in NAB alloys carries notable significance in marine environments. Biofouling, which entails the accumulation of marine organisms on submerged surfaces, directly influences the corrosion tendencies of NAB alloys²⁰. These microorganisms possess the capacity to trigger alterations in the alloy's electrochemical behavior, potentially accelerating corrosion processes²¹. The combined effects of corrosion and biofouling encompass the acceleration of localized attack, galvanic interactions, mechanical damage, and the formation of stagnation and concentration cells²². Thus, grasping the intricate interplay between biofouling and corrosion in NAB alloys is a complex endeavor, contingent upon factors such as the inherent nature of the marine environments and the eventual evolution of the alloy's microstructure. In addition, it is acknowledged that both the fabrication processes and post-heat treatment procedures hold profound influences over their ultimate microstructural configuration. Hence, numerous parameters, including the presence of microorganisms, the fabrication process, and post-heat-treatment processes, each play a distinct role in the corrosion resistance of NAB components within a marine environment. Given the significance of these factors, this study primarily aims to investigate the influence of manufacturing processes and subsequent heat-treatment procedures on the corrosion behavior of NAB alloy components in a 3.5 wt.% NaCl solution. This solution simulates the chloride ion concentration found in seawater but excludes the presence of microorganisms. Indeed, investigating the effects of manufacturing and post-heat-treatment processes on the corrosion behavior of NAB components provides essential insights. These insights are instrumental in comprehending the role of microorganisms in the degradation of NAB alloys when they are exposed to corrosive environments like the sea or ocean, paving the way for our subsequent research.

Taking these factors into account, the central objective of this paper is to thoroughly investigate the effects of combining WAAM with post-heat-treatment procedures on the corrosion performance of NAB alloys. In the previous work of our group, the microstructural features developed in the NAB-C95800 alloy fabricated by the GMAW-WAAM before and after heat-treatment processes were investigated¹⁴. It was found that the as-printed and heat-treated NAB parts' microstructures differ from those of the as-cast counterparts. Finding the effect of these differences on the corrosion performance of the as-built and post-processed WAAM parts is imperative for their applications in the industry to be an appropriate replacement for their conventional

manufactured counterparts. Hence, this investigation seeks to ascertain how the corrosion performance of NAB components, produced using the GMAW-WAAM approach, is influenced by both the additive manufacturing process and subsequent heat-treatment procedures.

RESULTS AND DISCUSSION

E-pH equilibria diagram

The Pourbaix diagrams (E (potential)-pH) related to the equilibrium reactions in the aqueous solution of 0.63 M NaCl and at the temperature of 25 °C are shown in Fig. 1 for the main alloying elements in the NAB sample, including Cu, Al, Ni, and Fe. Accordingly, the oxidation and dissolution reactions in an aqueous media at different electrochemical potentials and pHs are predicted thermodynamically using the Pourbaix plots. Thermodynamic calculations at different activities of ions were performed using the value of the standard chemical free energy data (G°). The Pourbaix diagrams were constructed using the database compiled in the HSC-06 software.

The Pourbaix diagrams illustrate the regions of stability for solid phases that are in equilibrium with each other or soluble species, and these regions are delineated using solid lines. In addition, the red dashed lines correspond to the chemical stability area of the water. The upper stability limit of water is based on the potential when the water is decomposed to the oxygen and H^+ ions in anodic reaction. Also, the hydrogen evolution on the cathode is related to the lower stability limit of the water. Furthermore, the finely spaced vertical lines positioned at pH = 7 within the Pourbaix diagrams depict the specific pH condition of the test solution utilized in this research. It is apparent from the E-pH diagram related to the Cu that the formation of Cu_2O and $Cu(OH)_2$ could occur predominantly at neutral pH following the anodic dissolution of Al to Al^{+3} and the formation of hydrated Al_2O_3 at the more positive potentials. The stability areas of the Ni $(OH)_2$ and Fe $(OH)_2$, FeO are also observed at the potential ranges between $-1.2 V_{Ag/AgCl}$ and $1.2 V_{Ag/AgCl}$ at pH of 7. In addition, the equilibrium potential between Cu/ Cu_2O is about $-0.2 V_{Ag/AgCl}$ according to the E-pH diagram of pure copper.

Cyclic potentiodynamic polarization (CPP) curves

Cyclic potentiodynamic polarization (CPP) measurements carried out on the as-built, heat-treated WAAM samples and the as-cast sample are illustrated in Fig. 2. All samples except the HT₃ showed an active-passive behavior in the test solution. Also, a distinct difference in corrosion current density (I_{corr}) is illustrated between the as-built WAAM specimen (A_1) and the rest of the specimens as shown in Fig. 2. However, the corrosion potential (E_{corr}) of the A_1 sample is slightly lower than the as-cast and the heat-treated samples, indicating the as-built NAB sample fabricated by the WAAM process is less noble than its counterpart cast sample and the heat-treated specimens.

Moreover, the corrosion density of current indicating the corrosion rate is almost of the same order of magnitude for the C_1 , HT₁, HT₂, and HT₃ samples. It is noted that the A_1 shows a wider pseudopassive area from the passivation potential (E_{pass}) about $-0.233 V_{Ag/AgCl}$ to $1.1 V_{Ag/AgCl}$ than that of the rest of the samples, and its value of the passive current (I_{pass}) is notably lesser compared to both the C_1 and the heat-treated WAAM samples. The electrochemical values (I_{corr} , E_{corr} , I_{pass} , and E_{pass}) are also displayed in Fig. 3. The E_{corr} considered as the open circuit potential (OCP) is also about $-0.293 V_{Ag/AgCl}$ for A_1 and an average of $-0.222 V_{Ag/AgCl}$ for the other samples, which are nearly reaching the equilibrium potential between Cu/ Cu^{+1} in form of Cu_2O (about $-0.2 V_{Ag/AgCl}$) shown in Fig. 1.

The Tafel slopes of the anodic branches of the CPP curves were also obtained and were in a range of 59–64 mV/decade. The

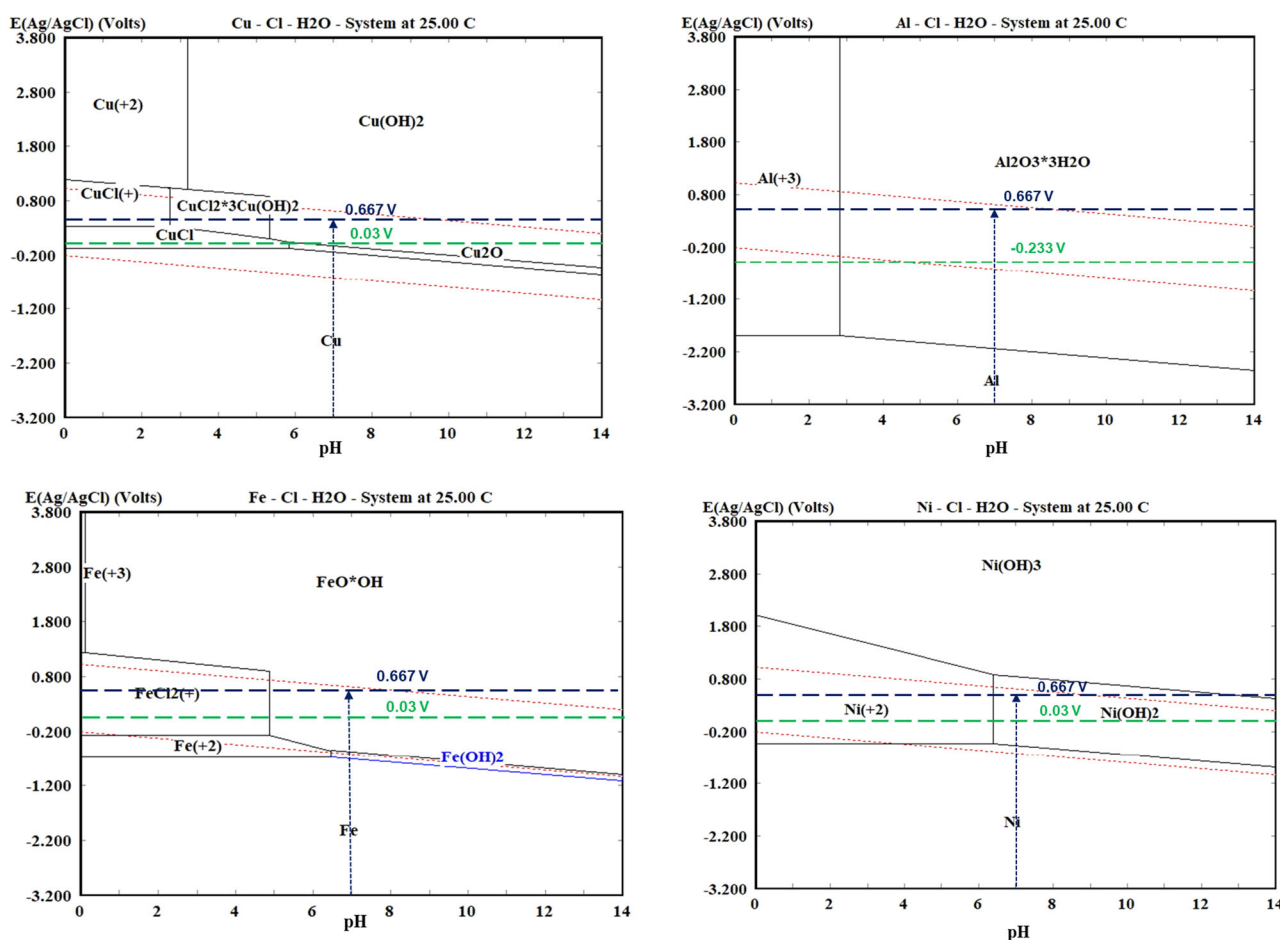


Fig. 1 Pourbaix diagrams of main alloying elements in NAB alloy. Pourbaix diagrams of Cu, Al, Ni, and Fe in the presence of 0.63 M Cl^- , equivalent to 3.5 Wt.% NaCl solution.

observed anodic Tafel slopes, which are ~ 60 mV/decade, might indicate the involvement of a diffusional process. This suggests that the dissolution process is governed by the diffusion rate of CuCl_2^{-1} species moving from the electrode surface across a diffusion layer²³. The influence of mass transfer on Tafel-like characteristics was also examined in chloride solutions as well as solutions containing other halides (X^-)^{24–26}. Consequently, when cuprous halide complexes (CuX_2^{-1}), which are stable soluble forms of copper, are present, the observed Tafel-like behavior is connected to the controlled potential-dependent concentration of these cuprous complexes at the outer Helmholtz plane (OHP) and their subsequent movement through the layer of diffusion^{27,28}. This condition resulted in a mass transport-kinetic control state in which the correlation between the potential and current density is expressed as follows for chloride solutions:²⁷

$$E(V_{SHE}) = E_{\text{CuCl}_2^-/\text{Cu}}^\circ + 0.059 \log \left(\frac{I \delta}{1000 F D_{\text{CuCl}_2^-}} \right) - 0.059 \log (a_{\text{Cl}^-})^2 \quad (1)$$

Here, $E_{\text{CuCl}_2^-/\text{Cu}}^\circ$ represents the standard equilibrium electrode potential between Cu and CuCl_2^{-1} . Meanwhile, $D_{\text{CuCl}_2^-}$ stands for the aqueous diffusion coefficient of cuprous chloride, F denotes Faraday's constant, a_{Cl^-} signifies the chloride activity, and δ refers to the diffusion layer's thickness at the copper surface. The passivation area of CPP curves with the reverse part is separately shown in Fig. 4 for more clarity on the forward and reverse sections. Accordingly, the forward and reverse sections of the CPP curves are shown as dashed lines and solid lines in Fig. 4, respectively. The forward section of the CPP diagrams in Fig. 4

showed the formation of a current peak near $0.07 V_{\text{Ag}/\text{AgCl}}$ and $0.03 V_{\text{Ag}/\text{AgCl}}$ (marked with a gray dash lined in Fig. 4) for the A_1 , and the rest of the samples (C_1 , HT_1 , and HT_2), respectively. There are also limiting current behavior at higher potentials related to the polarization behavior of the as-cast, HT_1 (350 °C) and HT_2 (550 °C) samples.

A comparison between the location of peak current near the $0.03 V_{\text{Ag}/\text{AgCl}}$ of the CPP curves and that on the copper Pourbaix diagram (displayed with a green dashed line in Pourbaix diagrams) implies the possibility of the initiation and expansion of the CuCl film on the NAB alloys' surfaces. Accordingly, a mass transport-kinetics process could control the formation and dissolution of the films on the alloy's surface. The dissolution rate of the surface films formed on NAB alloy exposed to the NaCl solution could be dependent on the rate of dissolution of CuCl film. In this regard, the CuCl dissolution depends on the diffusion of the CuCl_2^{-1} from the electrode surface through a diffusion layer. Moreover, a current peak close to $-0.233 V_{\text{Ag}/\text{AgCl}}$ is detected from the forward section of the CPP diagram related to the A_1 sample succeeded by a segment of diminished current across a limited potential span. This could be related to the dissolution of the Al element in the A_1 sample followed by the formation of Al_2O_3 , which is consistent with the region of the stability Al^{3+} ions and the formation of Al_2O_3 at the higher potentials from the Al Pourbaix diagram shown in Fig. 1. In addition, as the potential is made more anodic, the simultaneous dissolution of both Al and Cu, and other alloying components such as Ni and Fe, occur, resulting in the creation of complex films of the Al_2O_3 , $\text{Cu}_2\text{O}/\text{Cu}(\text{OH})_2$, $\text{FeO}(\text{OH})$, $\text{Ni}(\text{OH})_2/\text{Ni}(\text{OH})_3$ on the NAB alloys. A small bump

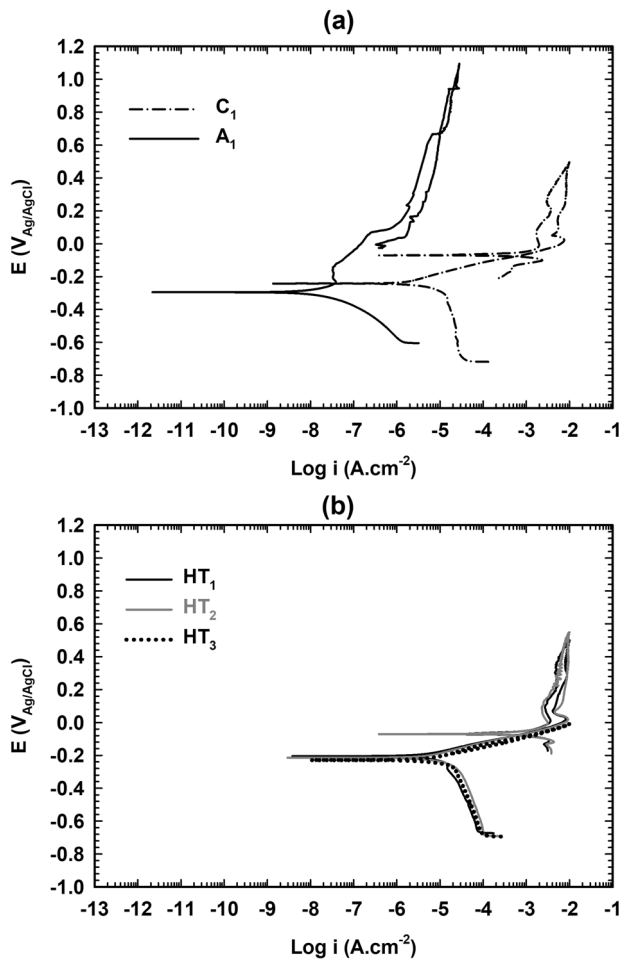


Fig. 2 Cyclic potentiodynamic polarization curves of the examined NAB samples exposed to a solution with a concentration of 3.5 wt.% NaCl at room temperature. **a** As-built WAAM and as-cast NAB samples, and **b** the WAAM samples after three different heat treatments (HT₁, HT₂, and HT₃).

of current was also observed from the anodic section for the A₁ sample at about 0.677 V_{Ag/AgCl}. The Pourbaix diagram of Cu implies this bump could be related to the formation of CuO, which is converted to the Cu(OH)₂ after hydration. In other words, it could be concluded that the Cu₂O is formed at the anodic potentials and oxidized to CuO at higher potentials²⁹. Subsequently, the CuO is hydrated to form Cu(OH)₂ on the surface of the alloy.

On the other hand, the CPP tests were conducted to assess the vulnerability of WAAM as-built and heat-treated NAB samples to pitting corrosion in comparison with their counterpart as-cast specimen. In these plots, the area enclosed by the hysteresis loop that forms signifies the degree of localized degradation experienced by the material. Moreover, if the density of current during backward scan surpasses that of the forward scan, it indicates a vulnerability to localized attacks, which could manifest as pit formation. Furthermore, the emergence of a negative hysteresis loop, where the current density during the reverse scan is lower than that during the forward scan, is indicative of the material's exceptional capacity to resist localized attacks³⁰. The observations of the forward and reverse sections of the CPP curves related to the C₁ (as-cast sample), and WAAM heat-treated samples, namely HT₁ and HT₂, reveal a similarity in the electrochemical responses exhibited by these specimens. The C₁, HT₁, and HT₂ samples show a wide passive-pseudopassive area from approximately 0.03 V_{Ag/AgCl} to 0.55 V_{Ag/AgCl}.

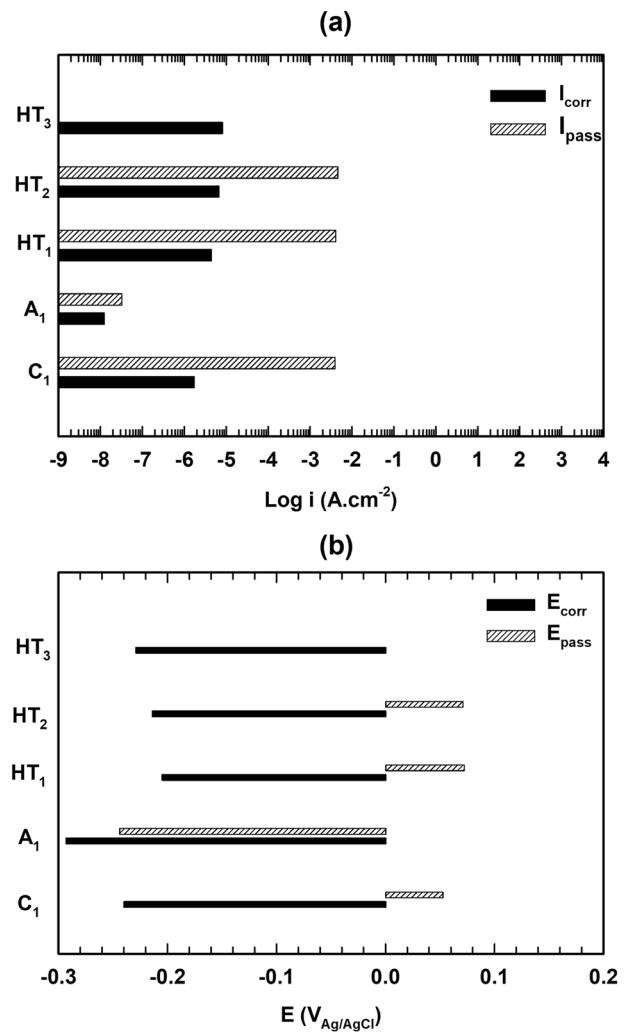


Fig. 3 Electrochemical values for the NAB samples. **a** Current parameters, and **b** potential parameters.

Notably, they lack a distinct pitting potential range, and a negative hysteresis during the reverse scan suggests a substantial ability to resist localized attacks in these particular samples. However, the HT₃ sample shows an active behavior relating to the formation of the oxide/hydroxide films before the polarization test. In other words, the point at which pitting begins aligns with the corrosion potential, resulting from the intersection of the cathodic branch with the transpassive zone of the anodic branch. At this juncture, the value of the potential related to pitting equates to the potential of corrosion, indicating higher susceptibility to localized attacks for the HT₃ sample.

Finally, the WAAM as-built sample (A₁) shows a passive-like stage extending from approximately -0.233 V_{Ag/AgCl} to -0.15 V_{Ag/AgCl}. Unlike the as-cast and the heat-treated samples, an increase in current follows to reach a passive-like area of about 0.667 V_{Ag/AgCl} to 1.1 V_{Ag/AgCl} with a relatively high current density suggesting the pseudopassivation. Hence, the rationale behind pseudopassivation stems from the creation of a surface layer that exhibits solubility in the external regions. Moreover, the negative hysteresis loop in the reverse scan is observed for the A₁, but it turns positive, intersecting the forward anodic scan at potentials slightly lower than the peak potential observed in the forward section. Therefore, the sample surface remains in the noble state, an indication that the repair of the pseudopassive films occurred easily in the potential just a few decades lower than the peak of the potential in

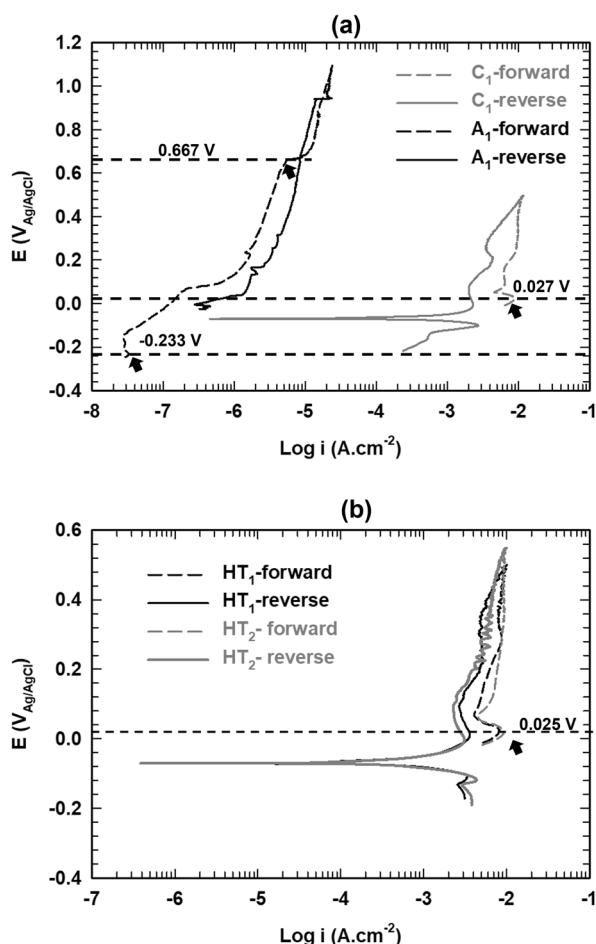


Fig. 4 A section of cyclic potentiodynamic polarization curves, including the passive area and the reverse section. **a** The A_1 and C_1 samples, and **b** for the HT_1 , HT_2 , and HT_3 specimens.

the forward scan. The pseudopassivation of the NAB samples also agrees with the formation of a complex structure of oxide/hydroxide from Al, Cu, Fe, Ni, and the presence of a CuCl film predicted from the Pourbaix diagrams. Accordingly, the formation of CuCl within the external layers of the surface films controls the rate of dissolution of the pseudopassive films established on the NAB samples' surface.

Microstructure observations and EIS measurements

Microstructural images of the as-cast (C_1), the WAAM as-built sample (A_1), and the heat-treated WAAM samples (HT_1 , HT_2 , and HT_3), are presented in Figs. 5a, d and 6a, d, g. Furthermore, the Nyquist and Bode plots of the specimens at OCP in the test solution are displayed in Figs. 5b, c, e, f and 6b, c, e, f, h, i. The SEM image of the C_1 sample depicted in Fig. 5a shows the evolution of the different intermetallic κ -phases precipitated in the interdendritic areas or the matrix of relatively coarse α -phase dendrites. It was detected from the present authors' earlier work that the κ_I rosette-shaped particles with a size of about 5–10 μm , κ_{II} with a globular morphology in the size of about 1–5 μm , and the κ_{III} phase in lamellar shape are formed in the interdendritic regions, while the fine particles of the κ_{IV} formed within the α -phase matrix¹⁴. Moreover, author's previous study on the microstructure of the NAB alloy showed that the microstructural features developed on the WAAM as-built specimen (A_1) are distinctly finer than those of its counterpart casting sample (C_1)¹⁴.

A section of a STEM-HAADF image of the A_1 sample with an inset of elemental map of Fe is presented in Fig. 5d to clarify the differences in the size of the α -dendrites as well as the intermetallic κ -particles in comparison with those formed in the as-cast sample. In contrast to the C_1 sample, the rosette-shaped particles of κ_I were not revealed in the interdendritic regions of the A_1 sample. In addition, TEM observations of the A_1 sample in our previous study showed the κ_{II} and κ_{III} phases are rich in alloying elements of Fe–Al as Fe_3Al and Ni–Al as Ni–Al, respectively, like those formed in the as-cast sample. Also, the TEM high magnification images defined the presence of fine nanometers of κ_{IV} intermetallic phase (5–10 nm) dispersed throughout the α -matrix. Also, the elemental maps taken from the TEM images showed the κ_{IV} precipitates are rich in Fe and Al like the κ_{II} phase.

Figure 6a, d, g displays the STEM images of the WAAM samples after three different heat-treatment processes. As seen from Fig. 6a, subsequent to subjecting the WAAM-NAB sample to a heat treatment of 350 °C for soaking of 2 h, only marginal modifications were observed in its microstructure. In other words, the microstructure features developed in the HT_1 sample are like those formed in the as-built sample (A_1). As this heat treatment did not result in any notable alterations in the microstructure, HT_1 can be safely employed on WAAM-NAB for stress-relieving purpose. The minor difference between the A_1 and HT_1 samples is related to the size of the κ_{IV} precipitates albeit without any discernible alteration in the volume proportion. The size of the κ_{IV} in the WAAM-NAB condition is varied in the range of 5–10 nm, whereas some coarsening occurred in HT_1 and the size is $\sim 10\text{ nm}$ ¹⁴. In contrast to HT_1 , the samples after HT_2 and HT_3 treatments performed at 550 °C—4 h and 675 °C—6 h showed an increase in the grain size from about 10 μm detected for the as-built and HT_1 to about 17 and 20 μm for HT_2 and HT_3 , respectively. Also, the TEM examinations of HT_2 and HT_3 samples shown in Fig. 6d, g reveal the presence of fine needle-like particles throughout the α -dendrites denoted as κ_V (Ni–Al based). However, the slender κ_V -precipitates within the α -dendrites of HT_3 exhibit a larger grain size (and significantly reduced precipitation) than those of the HT_2 sample. The elemental maps taken from the κ_V precipitates using STEM-HAADF revealed concentrated regions of Ni and Al, with some instances of substitutive Fe ($\sim 13\text{ wt}\%$). In addition, a lower number of κ_{IV} precipitates and observable coarsening of spherical κ_{II} precipitates were detected in both HT_2 and HT_3 when compared to the A_1 and HT_1 samples. Accordingly, the κ_{II} was also coarser in the HT_2 sample as compared to those precipitated in the HT_3 sample, and the κ_{III} morphology was to some extent converted from the lamellar to globular while a nearly complete transition from lamellar κ_{III} to globular particles occurred after the heat-treatment process at 675 °C for a soaking time of 6 h (HT_3). It is also noticeable that the HT_3 treatment resulted in less precipitation of κ_V particles, and more reduction of the κ_{IV} evolution compared to the HT_2 treatment.

Figures 5b, c, e, f and 6b, c, e, f, h, i show the Nyquist and Bode diagrams of all experimented NAB samples. The Nyquist plots of all samples are characterized by capacitive semicircles with two time constants at high-medium frequencies corresponding to the charge transfer reactions. Although a low-frequency tail related to a Warburg impedance is detected from the Nyquist curves for C_1 , A_1 , HT_1 , and HT_2 samples, the Nyquist plot of HT_3 sample retains its characteristic semicircular capacitive shape within the range of frequency. A comparison between the Nyquist plots shown in Figs. 5 and 6 revealed that the diameter of the capacitive semicircle of the WAAM as-built sample (A_1) is significantly higher than the rest of samples, indicating the higher resistance to electrochemical dissolution and the greater stability of the surface films³¹. In addition, the differences in the diameter of the semicircles of the as-cast, HT_1 , HT_2 , and HT_3 Nyquist plots appear to be low, indicating a slight difference in their electrochemical behavior

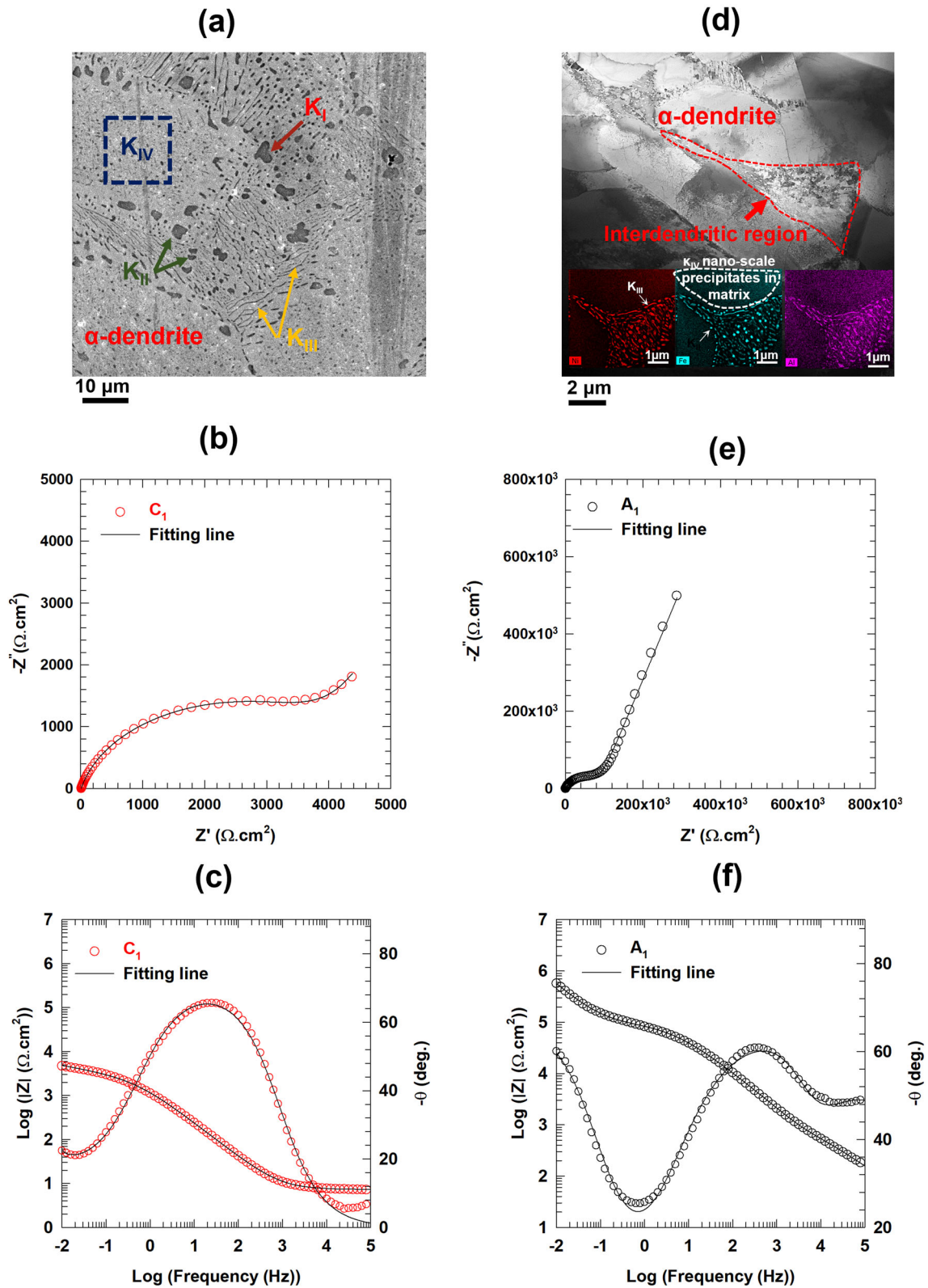


Fig. 5 Microstructural images and the EIS measurements of NAB samples. **a–c** Related to C_1 , and **d–f** related to A_1 samples, **a** SEM micrograph of C_1 , **b** Nyquist plot and **c** Bode plots for C_1 sample, **d** STEM-HAADF micrographs of A_1 with the inset of EDS elemental maps from Ni, Fe, Al, **e** Nyquist plot and **f** Bode plots for A_1 sample. EIS results are taken at OCP in a solution containing 3.5 wt.% NaCl.

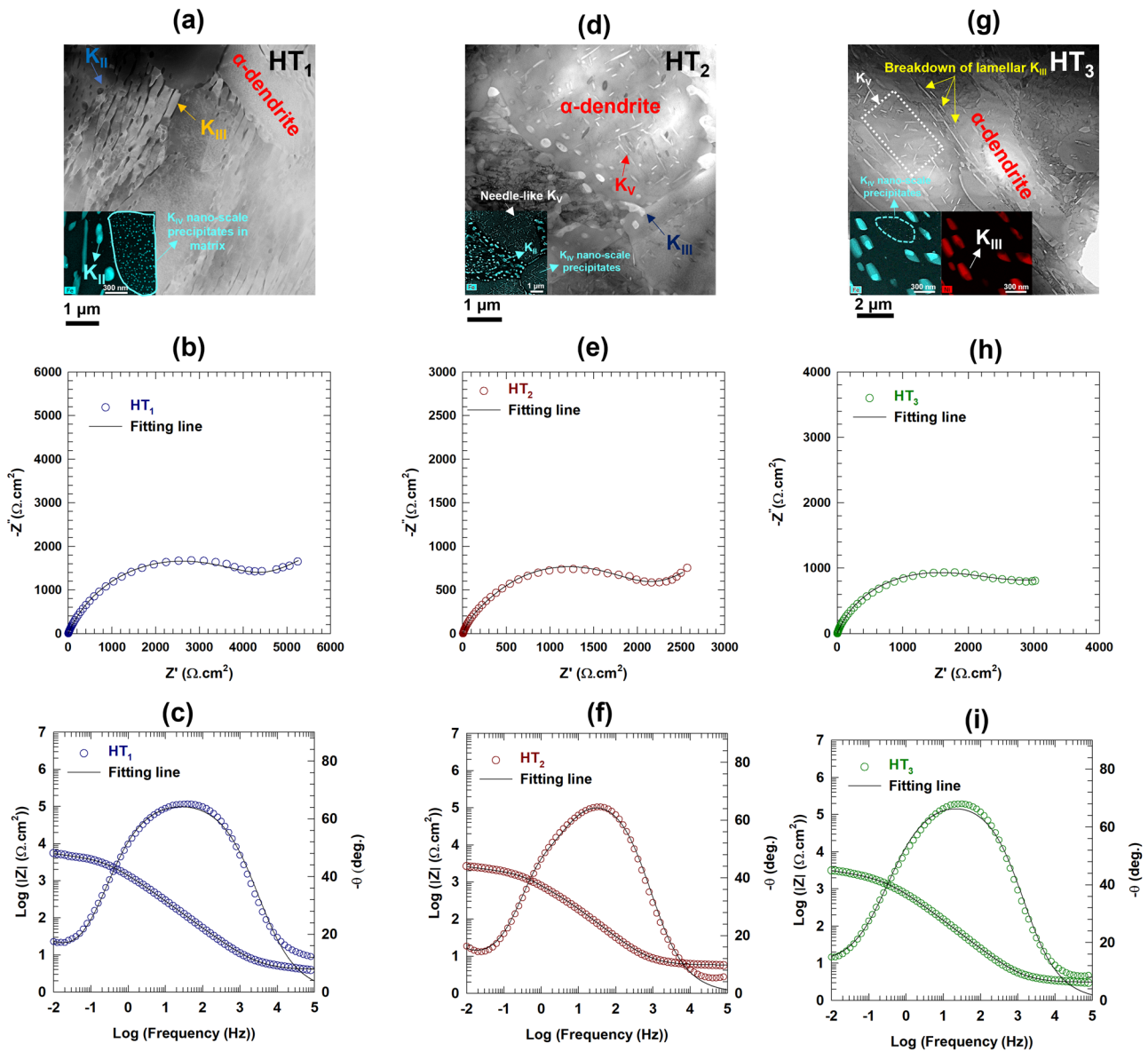


Fig. 6 STEM backscattered electron images and the EIS results of heat-treated NAB specimens. **a–c** Corresponds to HT₁, **d–f** corresponds to HT₂, and **g–i** corresponds to HT₃ samples, **a, d, g** STEM micrographs of HT₁, HT₂, and HT₃ with the inset of EDS elemental maps from Fe, and Ni elements, **b, e, h** Nyquist plots, **c, f, i** Bode plots taken at OCP in a solution containing 3.5 wt.% NaCl.

in the chloride solution. However, among as-cast and heat-treated samples, the highest value of the impedance modulus calculated at the lowest frequency from the Bode plots ($\text{Log } |Z|$ vs Log (frequency)) (Figs. 5 and 6) is related to the HT₁ sample. Also, a linear correlation between the $\text{Log } |Z|$ and Log (frequency) is observed in Bode modulus plots (Figs. 5c, f and 6c, f, i) over a wide range of frequency for all samples indicating the presence of semi-capacitance behavior in a wide range of the frequency.

The Bode phase plots of the as-cast and heat-treated samples correspond to a solitary, broad peak considered as a merging of two distinct time constants related to the passive-like films and capacitances of the double-layer. Accordingly, the separation of two time constants seems to occur from the Bode phase plot related to the A₁ sample. The A₁'s Bode phase plot shows a peak at the medium frequencies (about 2×10^2 Hz), and the evolution of another peak in its continuation to higher frequencies ($>10^5$ Hz) is predictable. Also, the maximum phase angles for all samples are about 61–69°, indicating the surface films generated on the NAB

samples' surfaces have a similar deviation of a pure capacitor³². The electrochemical phenomenon occurring at the sample surfaces is interpreted by fitting appropriate equivalent electrical circuit models (EEC) shown in Fig. 7a, b. The fitting results of the EIS data are also presented in Fig. 7c, d. The EEC models (EEC₁ and EEC₂) composed of two R // CPE elements were proposed to describe the behavior of passive-like films formed on the surface of the alloys as well as the charge transfer reactions focused on alloy's surface/solution. Moreover, a constant phase element to diffusion (CPE_w) was also added to the EEC₁ model (Fig. 7a) for the EIS data with a low-frequency tail ascribed to Warburg impedance³². In the EEC models, R_s shows the resistance of solution, R_f signifies the resistance of the passive-like film and R_{ct} is the resistance of charge transfer. The CPE_f and CPE_{dl} denote the passive film capacitance and double-layer, respectively. Also, CPE_w represents the electrical element considered for the finite-length diffusion process in the relevant EIS spectra. In such a case, the impedance (Z_{CPE}) and capacitance (T_w) of the CPE_w are given as

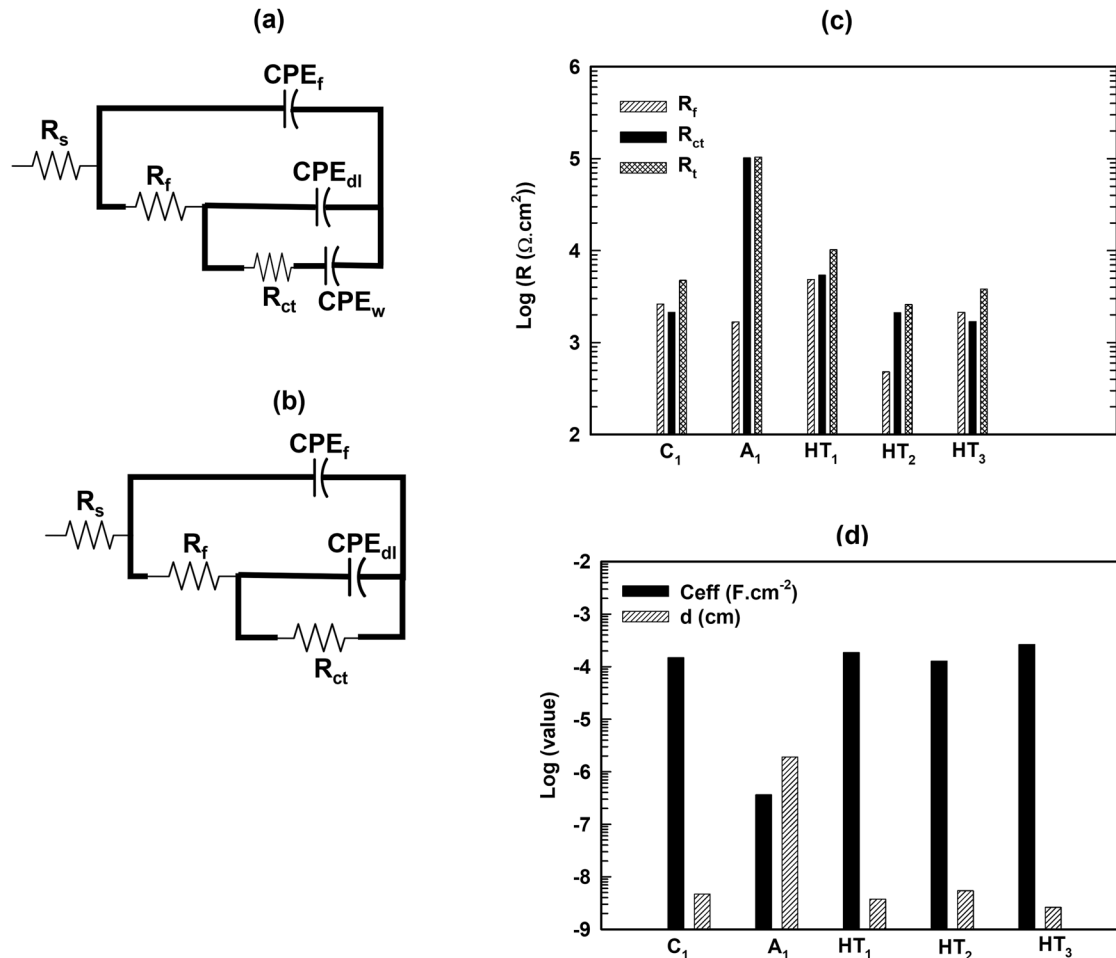


Fig. 7 EEC models and the electrochemical parameters derived by fitting the equivalent electrical circuit (EEC) models to the EIS data. **a** EEC₁ related to the EIS data of the A₁, C₁, HT₁, and HT₂ samples, **b** EEC₂ related to the EIS spectra of the HT₃ specimen, **c** the resistance parameters, and **d** the values of effective capacity and the thickness of passive-like films formed on the surface of the NAB alloy samples.

follows:³²

$$Z_{CPE_w} = \frac{\sigma' D_{diff}^{\phi_w - 0.5}}{(j\omega)^{\phi_w} \delta^{(2\phi_w - 1)}} = \frac{1}{(j\omega)^{\phi_w} T_w} \quad (2)$$

$$T_w = \frac{\delta^{(2\phi_w - 1)}}{\sigma' D_{diff}^{\phi_w - 0.5}} \quad (3)$$

where, D_{diff} is diffusion coefficient of the redox or oxidized species within the solution, j is $\sqrt{-1}$, ω represents angular frequency, ϕ_w stands for the dispersion coefficient related to surface inhomogeneity, and δ is diffusion layer thickness, and σ' is the mass transfer coefficient calculated as follows:³²

$$\sigma' = \frac{RT}{n^2 F^2 C_{diff} \sqrt{D_{diff}}} \quad (4)$$

In Eq. (4), T denotes the temperature (K), the gas constant (8.3144 J) is shown as R , n represents the number of electrons which are involved in the electrochemical reactions, F corresponds to the Faraday constant (9.6519×10^4 C), C_{diff} and D_{diff} represents the surface concentration and the diffusion coefficient of the diffusive species in the process. As shown in Fig. 7c, the total resistance, R_t was also presented for all samples using the summation of R_f and R_{ct} ($R_t = R_f + R_{ct}$). In addition, the effective capacity values (C_{eff}) and the passive-like film's thickness are displayed in Fig. 7d. The value of the effective capacity was calculated using the electrochemical parameters (R_f and the

capacitance of the CPE_f) fitted to the EIS spectra of the passive-like films^{33,34}. Moreover, the thickness of the passive film, which has an indirect relationship with the value of the C_{eff} ^{33,34} was also calculated and shown in Fig. 7d.

According to the resistance values shown in Fig. 7c, the total impedance (R_t) of the NAB alloys surface/passive-like film/solution system for the WAAM as-built sample (A₁), was about $103 \text{ k}\Omega \text{ cm}^2$ which is notably greater than the overall impedance of other samples. It was followed by the highest value of the passive-like film thickness ($d \sim 19 \text{ nm}$) in comparison with the as-cast and those subjected to heat treatment depicted in Fig. 7d. Moreover, the value of the R_t for the HT₁ sample ($\sim 10 \text{ k}\Omega \text{ cm}^2$) was about two times higher than the as-cast samples and about three to five times higher than the HT₃, and HT₂ samples, respectively. In addition, the HT₁ sample exhibited an elevated charge transfer resistance (R_{ct}) in comparison to the as-cast, HT₂, and HT₃ specimens, indicating the formation of higher barrier layers to the transfer of the electrochemical species on the surface of the HT₁ sample in contrast to the C₁, HT₂, and HT₃ specimens. The thickness of the oxide layers calculated for the C₁, HT₁, HT₂, and HT₃ samples are also almost the same values in a range of about 0.026 nm to 0.054 nm . These results suggest the oxide layers generated on the as-cast's surface and the WAAM samples after different heat treatments show a similar barrier property, however, the higher value of R_{ct} related to the HT₁ samples has a key role in raising the total resistance of the HT₁ surface to the corrosive

reactions in the test solution. Accordingly, it was also detected that the EIS spectra of A₁, C₁, HT₁, and HT₂ samples revealed a low-frequency region related to the diffusional processes in the test solution. The CPE_w related to the diffusional process was attributed to the low-frequency regions of the A₁, C₁, HT₁, and HT₂ samples.

The value of the capacitance of the CPE_w (T_w) as well as dispersion coefficient (ϕ_w) were also calculated for the samples and is depicted in Table 1. As shown in Table 1, the T_w value for the A₁ sample is the lowest (about $13.7 \mu\text{F cm}^{-2} \text{s}^{-1}$), indicating the highest resistance to diffusion of electrochemical species according to Eqs. (2) and (3). Also, the second lowest value of the CPE_w capacitance is related to the HT₁ sample (about $4021.1 \mu\text{F cm}^{-2} \text{s}^{-1}$), indicating the diffusional layer formed near the oxide layers created on the surface of HT₁ has the highest diffusional resistance among the C₁ and HT₂ samples.

Considering Eq. (1) and substituting the E and I values of the first current peak, which is about $0.03 V_{\text{Ag/AgCl}}$ in the forward

section of the CPP curves related to the HT₁, HT₂, and C₁ samples, as well as the insertion of the values of $D_{\text{CuCl}_2} \sim 1.2 \times 10^{-9} \text{ m}^2/\text{s}$, $\alpha_{\text{Cl}^-} = 0.478$ and $E_{\text{CuCl}_2/\text{Cu}} = 0.224 V_{\text{SHE}}$ into Eq. (1) give an average of the estimated δ values of about $2.5 \times 10^{-4} \text{ m}$. In addition, substituting the estimated δ value as well as the values of the ϕ_w , and T_w to Eq. (5) which is obtained from Eqs. (3) and (4) resulted in the finding of an estimation of the diffusion coefficient of the diffusional species which is about $5.2 \times 10^{-9} \text{ m}^2/\text{s}$ which is near the value of the diffusion coefficient of CuCl_2^- .

$$T_w = \frac{\delta^2 \phi_w^{-1} n^2 F^2 C_{\text{diff}}}{RT D_{\text{diff}} \phi_w^{-1}} \quad (5)$$

where T_w is the capacitance of the CPE_w, D_{diff} is diffusion coefficient of the redox or oxidized species in the solution, ϕ_w is the dispersion coefficient related to surface inhomogeneity, and δ represents the thickness of the diffusion layer. Also, the value of the C_{diff} was assumed to be related to the concentration of CuCl_2^- in the surface of the samples. The value of C_{diff} was calculated knowing the equilibria between Cu and CuCl_2^- as follows:



The surface morphologies of the as-built WAAM sample (A₁) and the sample which was heat-treated at 350 °C for 2 h (HT₁) after cyclic potentiodynamic polarization (CPP) testing in 3.5 wt.% NaCl solution are displayed in Fig. 8. Figure 8a highlights the interface area between the corroded regions of sample A₁ and its uncorroded area, marked with red broken lines. This indexed area in Fig. 8a is shown with a higher magnification image in Fig. 8b. In addition, Fig. 8c presents a higher magnification

Sample	T_w ($\mu\text{F cm}^{-2} \text{s}^{-1}$)	ϕ_w	$\chi^2 \times 10^3$
C ₁	5433.9	0.73	1.4
A ₁	13.7	0.76	0.78
HT ₁	4021.1	0.45	3.3
HT ₂	10502.0	0.67	2.3

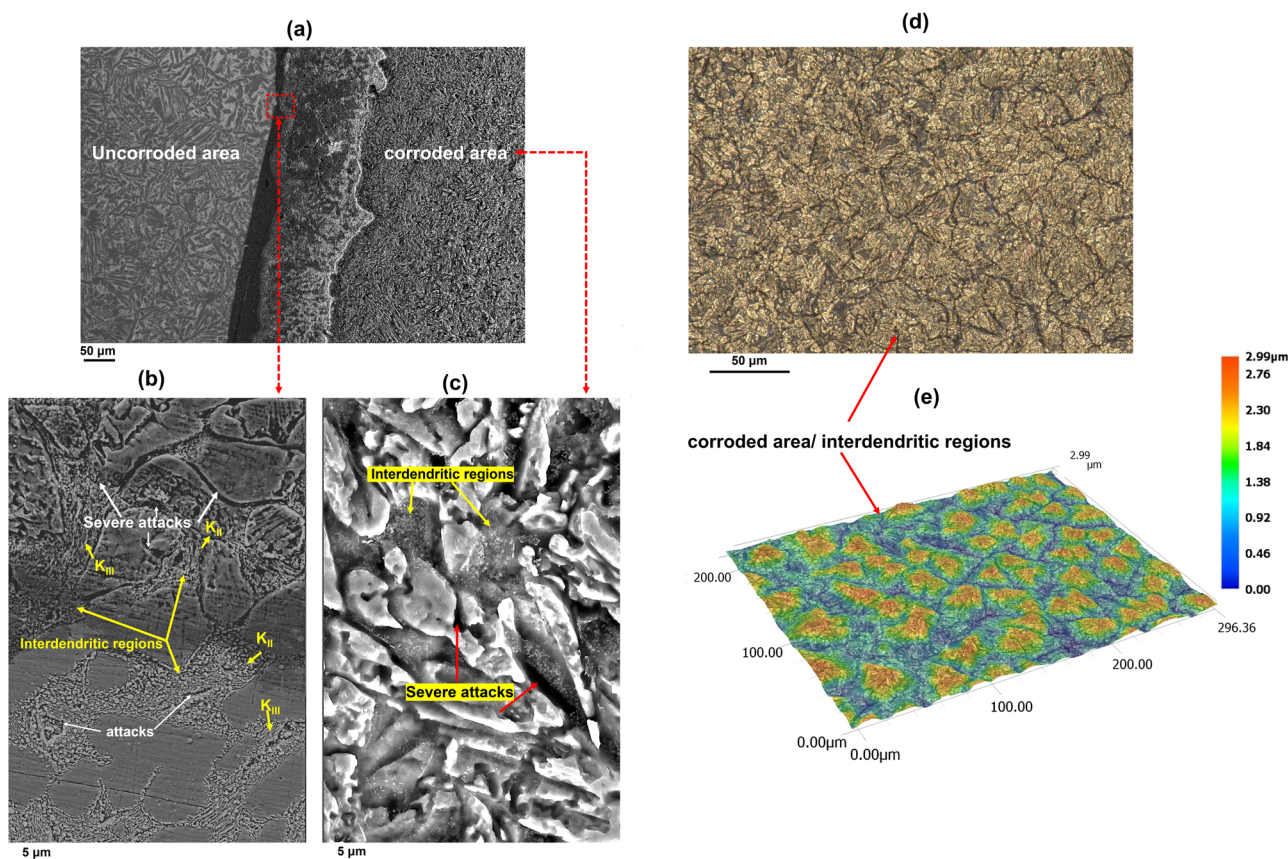


Fig. 8 micrographs of the surface structures of the A₁ and HT₁ specimens after corrosion tests. **a–c** SEM images of the surface of A₁ sample; **b, c** higher magnification images, **d, e** optical images of the corroded surface of HT₁ sample; **e** 3D image of the corroded surface of HT₁.

micrograph of the corroded area depicted in Fig. 8a. Throughout all areas of the corroded regions and the vicinity of the interface area, clearly visible localized areas exhibiting severe corrosion resembling in-depth cracks (marked with white and red arrows in Fig. 8b) are observed. However, the corrosive attacks are primarily localized in interdendritic regions. Notably, the corroded zones adjacent to the intermetallic precipitates of κ_{II} and κ_{III} are well observed from the SEM images.

The SEM observations of the corroded area with higher magnification (Fig. 8b) reveal that the Cu-rich matrix (α -dendrites) is also corroded uniformly and covered with corrosion products. However, the α -phase is more corroded in the interdendritic areas adjacent to the intermetallic κ -phases. The optical image from the HT₁ sample shows the presence of corrosion product on the α -phase and corroded areas in dark colors corresponding to the interdendritic regions (Fig. 8c). To assess the differences in the depth of corroded areas, a 3D image of the surface of the corroded area of the HT₁ sample was taken using a digital optical microscope, as shown in Fig. 8d. The severe attacks with a maximum surface depression depth of about 3 μm occurred in the interdendritic regions, resulting in the formation of Valley-like areas (blue color areas of Fig. 8e) near the peaks (uniformly corroded α -phases with the corrosion product). It is proposed that the intermetallic areas of κ -phases act as cathodic areas with respect to the α -phase, leading to severe attacks, particularly focused on the interdendritic regions where the α -phase corroded versus more noble precipitates of κ_{II} and κ_{III} phases. The presence of pits in the α -matrix is also noticeable, a result of the creation of microgalvanic cells between the κ_{IV} phase (acting as cathodes) and the matrix (acting as anode zones). It is worth noting that immersion in 3.5 Wt.% NaCl solution induces corrosive attacks localized in the α -phases adjacent to the intermetallic κ -phases, which are abundant in Fe, Al, and Ni (acting as the cathodic areas), irrespective of their morphologies. Thus, it can be confirmed that the size and number of κ -phases have a more significant impact on their electrochemical behavior compared to their morphologies. In other words, the morphological changes to κ -phases do not profoundly affect their affinity to corrosion reactions within a solution containing 3.5 Wt.% NaCl.

Deciphering: solidification structures and phase formation—corrosion correlation unveiled

Deciphering the effect of microstructural features on electrochemical behavior in the form of the corrosion performance can be complicated, especially if there are multiple phases and the different solidification structures from the columnar dendrites to equiaxed dendrites. Microstructural observations of the WAAM as-built sample (A₁) compared to those of the as-cast (C₁) showed that the higher cooling rates during the WAAM process led to significantly a finer dendritic structure than the casting process. It is reported that in conventional castings such as sand casting, typically used to fabricate the components of the NAB alloy, the cooling rate is at ~ 0.001 °C/s. This slow cooling rate hinders the formation of a finer microstructure when compared to the WAAM process, which boasts a significantly higher cooling rate, exceeding 1 °C/s^{35,36}.

In addition, the equiaxed dendrites were also detected on the primary columnar dendrites of α -phase in the sample of NAB produced by the WAAM process. Moreover, the higher cooling rate of the WAAM process suppresses the formation of the κ -rosette-shaped particles in the interdendritic regions due to the lack of sufficient time for the partitioning of alloying elements. Besides the microstructural results, the CPP measurements of the NAB samples indicated, the A₁ sample has the lowest value of the current density of corrosion (i_{corr}) in comparison with the other samples. However, the value of E_{corr} of A₁ sample was lower than the as-cast and the heat-treated samples. The lowest value of i_{corr}

for the A₁ sample compared to the other samples can be related to finer equiaxed dendritic structures developed during the solidification process. It is well-known the value of i_{corr} depends on the current density exchange value (i_0) indicating the kinetic aspects of the corrosion phenomenon. Accordingly, i_0 has a direct relationship with the surface roughness as an index for an augmentation in the exposed area³⁷.

During the columnar dendrite growth of the α -phase as a copper-rich constituent, the surface roughness of the anodic area increases, and could cause an increase in the surface area, resulting in augmentation of the corrosion and other surface-dependent reactions on the surface of alloy. Therefore, the reduction of surface area with the evolution of a finer and more equiaxed dendritic structure in the as-built NAB sample fabricated using AM technique could be one of the critical parameters to decrease the value of i_0 of the redox reactions on its surface, resulting in a lower corrosion current density compared to the as-cast and the heat-treated NAB specimens. In addition, the less nobility of the E_{corr} for the A₁ compared to the rest of the specimens attributed to the precipitation of finer interdendritic and dendritic κ -phases with lower amounts than those formed in the other samples as well as the absence of the κ_I particle in the microstructure of the A₁ sample. It was previously reported that the Fe, Ni, Al-rich κ -phase are more cathodic than the copper-rich α -phase¹⁹.

Deciphering: heat-treatment process—corrosion correlation unveiled

The study of the microstructural changes after heat-treatment processes on the WAAM-NAB samples also revealed the stress-relief treatment (HT₁) resulted in a slight change of the microstructural features developed after WAAM process in which the only change was related to slight increase in the size of κ_{IV} particles. Accordingly, the growth of the Fe–Al-rich (Fe₃Al based) κ_{IV} precipitates during the HT₁ treatment affect resistance to corrosion of the HT₁ sample. The higher work function of Fe and Ni compared to that of the Cu lead to higher nobility of the Fe–Al and Ni–Al-rich phases than the α -phase which is a Cu-rich phase. Accordingly, HT₁ treatment induced a larger cathodic area to anodic area in the NAB sample, which lead to an acceleration of the microgalvanic reactions resulting in an elevated rate of corrosion^{38,39}. In this regard, it was also detected that the formation of Ni–Al and some extent Fe-rich κ_V phases in the matrix of HT₂ and HT₃ samples accompanied by the grain growth in the dendritic structure as well as coarsening of the κ_{II} precipitates had a detrimental impact on their corrosion performances obtained from the CPP and EIS results.

The evolution of another cathodic phase (κ_V) in the needle-like shape as well as coarsening of the Fe–Al-rich κ_{II} phase as the cathodic area versus the anodic α -dendritic matrix promote the formation of microgalvanic cells which increase the electron exchanges between the cathodic and anodic reactions performed on these areas of the HT₂ and HT₃ samples. However, the breakdown of the lamellar κ_{III} phase to a completely spheroidized morphology in the HT₃ sample positively affects its resistance to corrosion in comparison with the HT₂ specimen. The value of R_t calculated from the EIS results related to the HT₂ and HT₃ confirmed a slightly higher corrosion resistance of the HT₃ specimen than that of the HT₂ sample.

Deciphering: formation of surface films on NAB alloy

In addition, the observations of the cyclic potentiodynamic polarization parameters and the potential-pH thermodynamic diagrams of the corrosion reactions in the aqueous media as Pourbaix diagrams proposed the evolution of a complex pseudopassive films consisted of primarily from the Al₂O₃, Cu₂O, Cu(OH)₂, and the oxide/hydroxides of Ni and Fe on the surface of

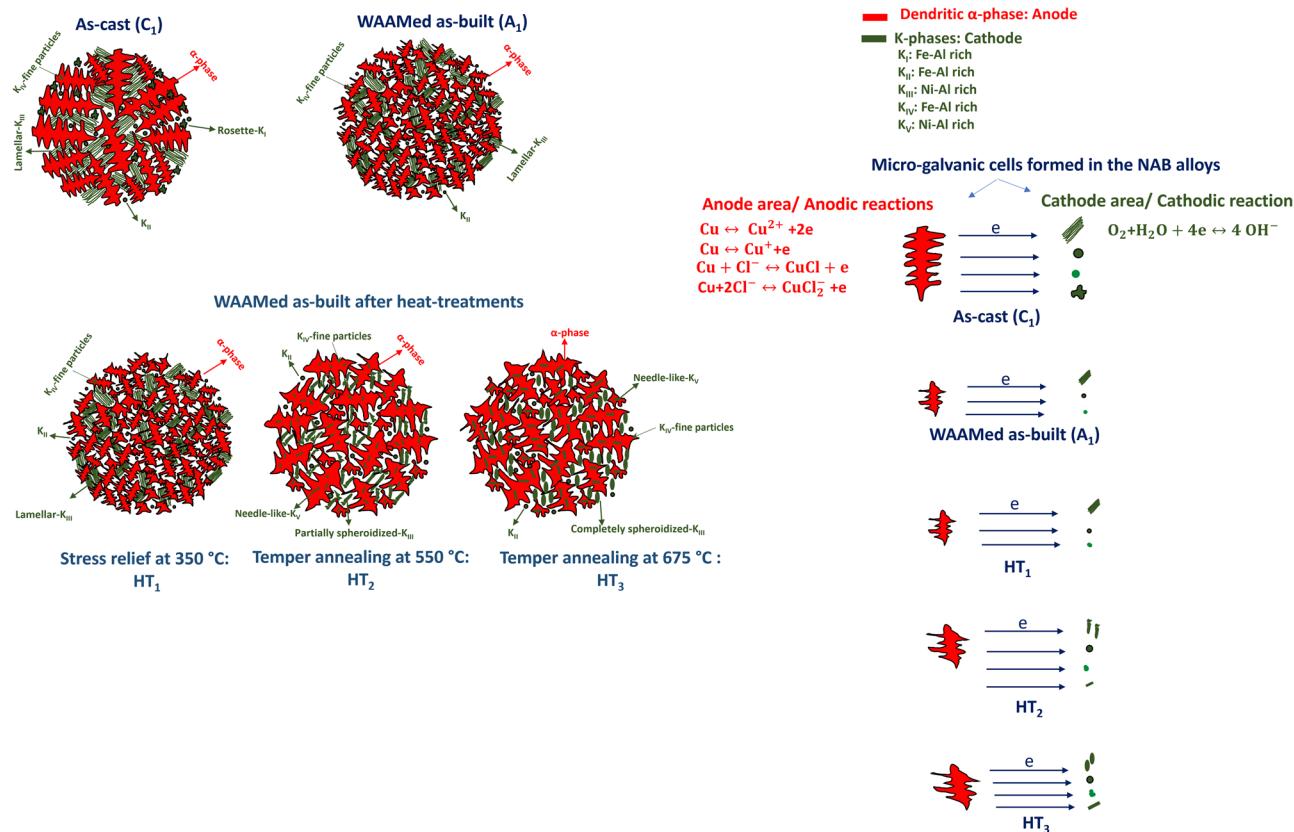


Fig. 9 Schematic illustration of corrosion behavior of the NAB samples in the chloride-containing environment. The formation of κ -phases triggers the formation of microgalvanic cells, drawing more galvanic currents.

the NAB alloys with the presence of a $CuCl$ film formed on the outer layer of the passive-like films at neutral $NaCl$ solution. It is also implied that the surface films consist of an inner layer with highly protective properties associated with the creation of the Al_2O_3 on the α -matrix and the Al-rich intermetallic phases (κ -phases), as well as an outer layer enriched in cuprous oxide/hydroxides^{2,40}. In addition, the calculated Tafel slopes from the anodic branches of CPP curves fall in the range, which is related to a mass transport control mechanism occurring near the surface. Accordingly, the presence of a mass transport control or diffusional mechanism which controls the dissolution of the surface films formed on the NAB alloy was confirmed by observing a low-frequency tail related to a Warburg impedance form the EIS spectra A_1 , C_1 , HT_1 , and HT_2 samples. Substituting the experimental parameters (I and E) obtained from the CPP curves in Eq. (1) resulted in the determination of the diffusional layer thickness formed near the outer layer of the films.

The insertion of the EIS parameters related to the low frequencies' region, T_w , and ϕ_w in Eq. (5) with the calculated thickness of the diffusional layer (δ) from Eq. (1), gave the estimation of the value of diffusion coefficient of the redox or oxidized species (D_{diff}) which was equal to the value of the diffusion coefficient of $CuCl_2$ confirming the role of the cuprous chloride in controlling the degradation of passive-like films formed on the NAB surface alloys.

Corrosion mechanism in NAB alloy

Figure 9 displays a scheme of the corrosion mechanism in the NAB alloys. The correlation between the microstructural features developed in the as-cast, WAAM as-built before and after three different heat-treatment processes is briefly shown in Fig. 9. Accordingly, the microgalvanic cells formed between the α -phase

as anode area versus the κ -phases as the cathodic regions in the NAB samples. The presence of more cathodic areas in the as-cast and the heat-treated samples, which consume more electrons produced from the anodic reactions, lead to a higher current density. Although the morphology of the lamellar κ_{III} phases was also partially and completely converted to a spheroidized shape after heat treatment at 550 °C for a soaking time of 4 h and heat treatment at 675 °C for a soaking time of 6 h, respectively, evolution of a higher cathodic areas in those samples lead to their inferior corrosion resistance in comparison with the WAAM as-built (A_1) and the HT_1 sample (350 °C for 2 h).

In the continuity of our previous research group's studies on microstructural features developed in nickel–aluminum bronze (NAB) parts fabricated by wire arc additive manufacturing (WAAM) technique before and after three different heat-treatment processes, namely HT_1 , HT_2 , and HT_3 , the performance of corrosion of the WAAM components in the form their as-built state and after undergoing heat treatment were investigated. In addition, the corrosion behavior of the WAAM parts compared with their counterpart cast component in a solution containing 3.5 Wt.% $NaCl$ in the current research. The correlation between these microstructural changes and corrosion behavior in WAAM-NAB-C95800 can be summarized as follows:

1. The suppression of the formation of κ_I -rosette-shaped particles and the evolution of a finer and more equiaxed dendritic α -phase as the matrix after the WAAM process mainly improved the corrosion resistance of the NAB components. The κ -phases in the form of Ni–Al-rich (κ_{III} and κ_V) or Fe–Al-rich (κ_{II} , κ_{IV}) intermetallic components played a cathodic role versus the α -dendritic matrix enriched from the copper element, which acts as the anode area in the neutral chloride solution.

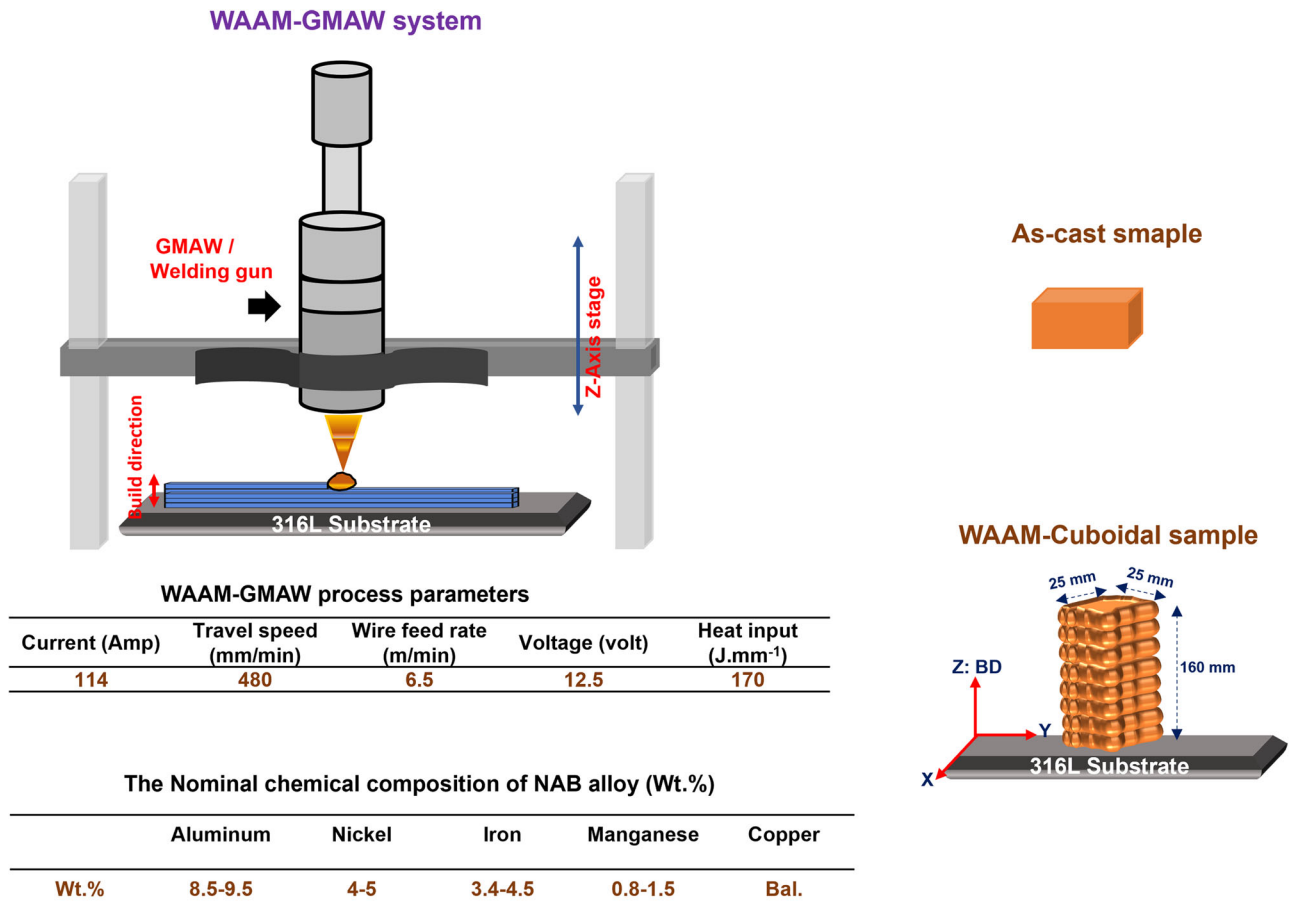


Fig. 10 Schematic fabrication process and NAB sample details. GMAW-WAAM technique, its process parameters, the square bar fabricated by WAAM, the bar-shaped as-cast component cut from an impeller for the corrosion study, and the chemical composition of the NAB alloy.

- The coarsening of κ_{IV} particles after applying the HT₁ treatment (350 °C for 2 h) reduced the corrosion resistance of the WAAM component significantly. However, the reduction of the corrosion performance observed from the electrochemical parameters obtained from cyclic potentiodynamic polarization (CPP) and EIS tests confirmed the treatments at 550 °C and 675 °C (HT₂ with $i_{corr} \sim 6.6 \times 10^{-6} \text{ A cm}^{-2}$ and $R_t \sim 2.58 \text{ K}\Omega \text{ cm}^2$, and HT₃ with $i_{corr} \sim 8 \times 10^{-6} \text{ A cm}^{-2}$ and $R_t \sim 3.8 \text{ K}\Omega \text{ cm}^2$) exert a more adverse influence on the corrosion behavior of the WAAM-manufactured samples when contrasted with the influence of HT₁ (i_{corr} about $4.4 \times 10^{-6} \text{ A cm}^{-2}$ and R_t about $10.2 \text{ K}\Omega \text{ cm}^2$) on the performance of corrosion of the parts of NAB produced by WAAM process.
- The precipitation of an additional cathodic phase of the κ_V in needle morphology had a pivotal role in decreasing the performance of corrosion of the components, which were heat-treated at 550 °C for a soaking time of 4 h (HT₂) and 675 °C for a duration of 6 h (HT₃). However, the conversion of the κ_{III} phase to a completely spheroidized morphology has a positive effect on the corrosion resistance of the HT₃ part compared to that of the HT₂ component.
- The corrosion current density and total impedance modulus of the heat-treated samples were almost the same as those of the as-cast NAB part, indicating the as-built state of the WAAM parts has a superior corrosion resistance than the heat-treated and as-cast parts due to the formation of a lower and finer κ -phases.
- The partial and complete conversion of lamellar to spheroidized morphology in the κ_{III} phase after treatments at 550 °C and 675 °C did not improve the corrosion performance.
- Comparison of the polarization behavior of the NAB alloy in the natural NaCl solution (pH about 7) with the Pourbaix diagrams of copper, aluminum, iron, and nickel showed the anodic behavior was consistent with the initiation and expansion of the CuCl film on the surface of the NAB alloys.
- The apparent anodic Tafel slopes calculated for the NAB alloy from the forward section of the CPP curves as well as the formation of a low-frequency tail related to a Warburg impedance in the EIS spectra confirmed the presence of mass transport-kinetics process in which dissolution of the outer surface layers governed by the rate at which the CuCl_2^- ions diffuse across a diffusion layer.

METHODS

Materials and GMAW-WAAM process

NAB alloy specimens in this study were cut from the as-cast specimen, and the schematic of the WAAM fabricated sample is shown in Fig. 10. Gefertec, headquartered in Berlin, Germany, utilized their 3DMP (3D metal printing) technology to fabricate the WAAM samples in square bar shapes. The NAB samples were produced through a manufacturing process based on gas metal arc welding (GMAW) utilizing the WAAM technique. Figure 10

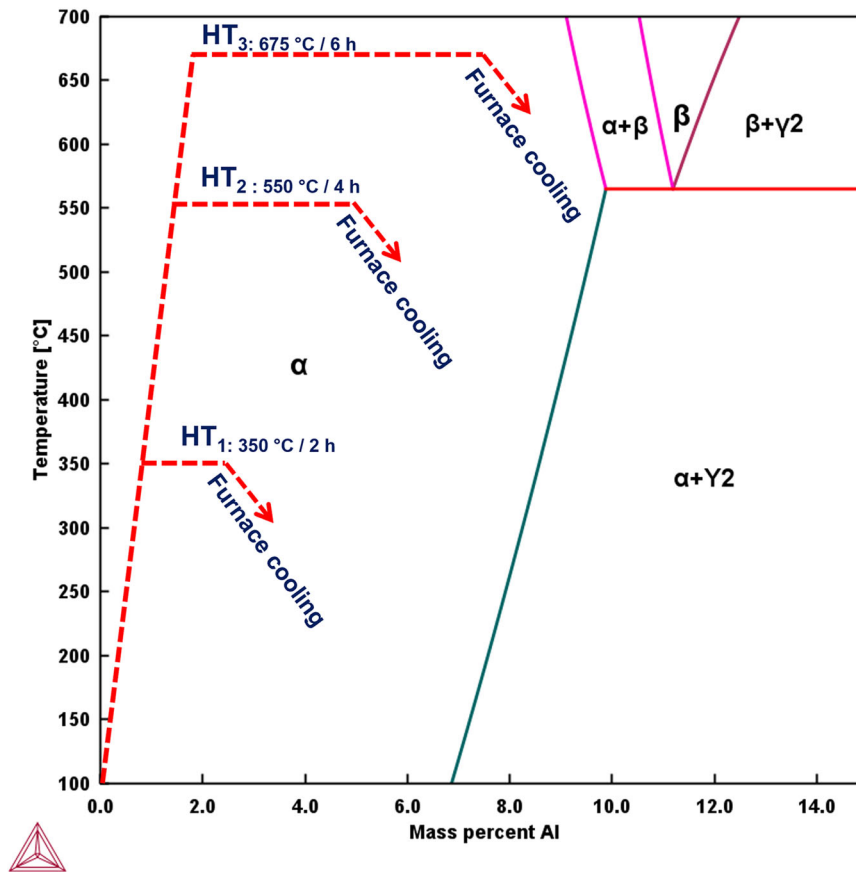


Fig. 11 A visual representation outlining three different heat treatments applied to the NAB component fabricated by WAAM process. illustration of three different heat-treatment processes is also superimposed to the binary Cu–Al phase diagram.

illustrates a schematic representation of the GMAW-WAAM system employed in the present investigation. NAB filler wires (A5.7 ERCuNiAl) were melted out and deposited over a 316L stainless (SS) substrate with a 10 mm thickness. Also, the GMAW welding torch perpendicular on the substrate was installed to fabricate a square bar with the dimensions displayed in Fig. 10. Inert shielding gas as an integral part of GMAW-WAAM was also purged to the system to protect/provide a shield over the melt pools. The optimized process parameters based on the fabrication of the intact samples were applied in this process and displayed in Fig. 10. The chemical composition details of the NAB-C95800 samples is also provided in Fig. 10.

Heat treatment and microstructural characterizations

Heat-treatment processes were also applied to cuboidal samples cut from the middle section of the square bar fabricated using the GMAW-WAAM technique. The cuboidal specimens were heated into different temperatures as shown in Fig. 11. The heat-treated samples were named as HT₁, HT₂, and HT₃. HT₁ was considered a stress-relief treatment and performed at 350 °C for 2 h. Two other heat-treatment cycles were also applied to two other cuboidal samples denoted HT₂ and HT₃. Accordingly, HT₂ is related to heat treatment at 550 °C for 4 h and HT₃ is attributed to a heat treatment at 675 °C for 6 h. All heat-treated samples were cooled until room temperature in a furnace with a cooling rate of about 8–20 K/min. A section of the Cu–Al binary phase diagram calculated using ThermoCalc software is illustrated in Fig. 11. Under equilibrium conditions, it is observed that the binary alloys comprising aluminum up to a concentration of 9% constitute a singular phase known as the α solid solution at ambient temperature. Furthermore,

a secondary phase denoted as β becomes evident within the microstructure. Additionally, these alloys experience a phase transition at 565 °C during gradual cooling. Notably, a eutectoid reaction takes place in these alloys, leading to the transformation of the β phase into an α and γ_2 eutectoid structure. However, adding the Ni and Fe to binary alloys of Cu–Al suppresses the formation of γ_2 , and instead of γ_2 , κ -phases could be precipitated in the matrix. The location of temperatures for the heat-treating processes is also superimposed into the binary plot of the Cu–Al alloy.

Microstructural analyses were also conducted on the surface that is oriented perpendicular to the fabrication direction of the GMAW-WAAM samples (shown in Fig. 10). Moreover, as-cast samples were cut from a NAB saltwater impeller (the diameter of the impeller was 170 mm) to consider as the reference sample in this study. A Scios dual-beam scanning electron microscope (SEM) and FEI Tecnai Osiris Transmission Electron Microscope (TEM) were employed to characterize the microstructural features developed in the samples. After mounting and mechanical polishing, samples were chemically etched using a Klemm's reagent for about 30 s to be prepared for the SEM observations. Moreover, the GMAW-WAAM samples were reduced to approximately 30 μm thickness utilizing the ion-beam milling technique. This preparation was performed using a Gatan Precision Ion Polishing System (PIPS, model 695) operating at an accelerating voltage of 200 kV, ensuring their suitability for TEM examinations. Additionally, elemental distribution maps were generated by combining energy dispersive spectroscopy (EDS) with high-angle annular dark-field (HAADF) detectors. The samples were also denoted as follows:

As-cast specimen: C₁, specimen cut from the GMAW-WAAM square bar: A₁, and the heat-treated samples were named as HT₁, HT₂ and HT₃.

Electrochemical tests

The surface of the samples for electrochemical tests were ground to achieve a polished surface with a reflective appearance. The specimens were cleansed using distilled water and pure ethanol. Then the samples were quickly dried by hot air and transferred to the naturally aerated 3.5 wt.% NaCl solution. The surface area exposed on the specimens ranged from ~0.181 to 1.171 cm². All electrochemical assessments took place at an ambient temperature of around 23 ± 2 °C, utilizing a potentiostat/galvanostat (Gamry model reference 600 +), in a cell including three-electrodes, where the GMAW-WAAM and as-cast NAB samples were considered as the working electrode (WE), while a graphite rod served as the counter electrode (CE), and a saturated silver/silver chloride (Ag/AgCl) electrode functioned as the reference electrode (RE). Before the corrosion examinations, the stable open circuit potential (OCP) of the specimens was observed over a duration of 1800 seconds. Subsequently, electrochemical impedance spectroscopy (EIS) was performed using an alternating signal possessing a 10 mV amplitude, encompassing a frequency spectrum from 100 kHz to 0.01 Hz. In addition, cyclic potentiodynamic polarization (CPP) measurements were conducted by sweeping the potential at a rate of 0.166 mV/s. The range of potential extended from 500 mV below the OCP to the point where the density of current reached 10 mA/cm², followed by a reverse sweep back to the initial point. The corrosion tests were connected to the surface of the samples as follows:

1. After 96 h of immersion of as-built WAAM sample A₁ and the as-cast specimen (C₁) in 3.5 wt.% NaCl solution.
2. After 24 h of immersion of the heat-treated samples within 3.5 wt.% NaCl solution.

Finally, the EIS tests were conducted at OCP, and the Zview software was used to analyze and fit the proper curves to the experimental EIS results. The surface morphology of the samples after corrosion tests were also observed with an Scios 2 dual-beam scanning electron microscope (SEM) through a field emission mode and optical microscope (Keyence digital microscope vhx-7000 series).

DATA AVAILABILITY

The datasets generated during and/or analyzed during the current study are available from the corresponding author upon reasonable request.

Received: 12 August 2023; Accepted: 13 October 2023;
Published online: 27 October 2023

REFERENCES

1. Richardson, I. *Guide to Nickel Aluminium Bronze for Engineers* (Copper Development Association, 2016).
2. Schüssler, A. & Exner, H. E. The corrosion of nickel-aluminium bronzes in seawater —i. protective layer formation and the passivation mechanism. *Corros. Sci.* **34**, 1793–1802 (1993).
3. Park, J.-C., Han, M.-S. & Kim, S.-J. Investigation on the cavitation damage behavior with temperature and cavitation time in seawater. *Surf. Interface Anal.* **44**, 1407–1410 (2012).
4. Yang, F. et al. The role of nickel in mechanical performance and corrosion behaviour of nickel-aluminium bronze in 3.5 wt.% NaCl solution. *Corros. Sci.* **139**, 333–345 (2018).
5. Yao, C.-L. & Shim, D.-S. Corrosive properties of cuni2sic fabricated through directed energy deposition on a nickel-aluminum bronze substrate. *J. Alloys Compd.* **918**, 165776 (2022).
6. Cottam, R. & Brandt, M. Laser surface treatment to improve the surface corrosion properties of nickel-aluminum bronze. In J. Lawrence and D.G. Waugh (eds) *Laser Surface Engineering* 469–481 (Woodhead Publishing, 2015).
7. Xu, C. et al. Corrosion behavior of wire-arc additive manufactured and as-cast Ni-Al bronze in 3.5 wt% NaCl solution. *Corros. Sci.* **215**, 111048 (2023).
8. Pattanayak, S. & Sahoo, S. K. Gas metal arc welding based additive manufacturing —a review. *CIRP J. Manuf. Sci. Technol.* **33**, 398–442 (2021).
9. Suryakumar, S. et al. Weld bead modeling and process optimization in hybrid 14layered manufacturing. *CAD* **43**, 331–344 (2011).
10. Song, Y.-A. & Park, S. Experimental investigations into rapid prototyping of composites by novel hybrid deposition process. *J. Mater. Process. Technol.* **171**, 35–40 (2006).
11. Bambach, M., Sizova, I., Sydow, B., Hemes, S. & Meiners, F. Hybrid manufacturing of components from Ti-6Al-4V by metal forming and wire-arc additive manufacturing. *J. Mater. Process. Technol.* **282**, 116689 (2020).
12. Li, Y., Han, Q., Horváth, I. & Zhang, G. Repairing surface defects of metal parts by groove machining and wire + arc based filling. *J. Mater. Process. Technol.* **274**, 116268 (2019).
13. He, T., Yu, S., Shi, Y. & Huang, A. Forming and mechanical properties of wire arc additive manufacture for marine propeller bracket. *JMP* **52**, 96–105 (2020).
14. Dharmendra, C., Rice, K. P., Amirkhiz, B. S. & Mohammadi, M. Atom probe tomography study of k-phases in additively manufactured nickel aluminum bronze in as-built and heat-treated conditions. *Mater. Des.* **202**, 109541 (2021).
15. Culpan, E. A. & Rose, G. Corrosion behaviour of cast nickel aluminium bronze in sea water. *Br. Corros. J.* **14**, 160–166 (1979).
16. Al-Hashem, A., Caceres, P. G., Riad, W. T. & Shalaby, H. M. Cavitation corrosion behavior of cast nickel-aluminum bronze in seawater. *Corrosion* **51**, 331–342 (1995).
17. Wharton, J. A. & Stokes, K. R. The influence of nickel-aluminium bronze microstructure and crevice solution on the initiation of crevice corrosion. *Electrochim. Acta* **53**, 2463–2473 (2008).
18. Neodo, S., Carugo, D., Wharton, J. A. & Stokes, K. R. Electrochemical behaviour of nickel-aluminium bronze in chloride media: Influence of ph and benzotriazole. *J. Electroanal. Chem.* **695**, 38–46 (2013).
19. Song, Q. N., Zheng, Y. G., Ni, D. R. & Ma, Z. Y. Studies of the nobility of phases using scanning kelvin probe microscopy and its relationship to corrosion behaviour of ni-al bronze in chloride media. *Corros. Sci.* **92**, 95–103 (2015).
20. Dou, W. et al. Investigation of the mechanism and characteristics of copper corrosion by sulfate reducing bacteria. *Corros. Sci.* **144**, 237–248 (2018).
21. Mansfeld, F. & Little, B. Microbiologically influenced corrosion of copper-based materials exposed to natural seawater. *Electrochim. Acta* **37**, 2291–2297 (1992).
22. Huang, G., Chan, K.-Y. & Fang, H. H. P. Microbiologically induced corrosion of 70Cu-30Ni alloy in anaerobic seawater. *J. Electrochem. Soc.* **151**, B434 (2004).
23. Tromans, D. & Silva, J. C. Behavior of copper in acidic sulfate solution: comparison with acidic chloride. *Corrosion* **53**, 171–178 (1997).
24. Smyrl, W. H. Electrochemistry and corrosion on homogeneous and heterogeneous metal surfaces, electrochemical materials science. In J. O'M. Bockris, Brian E. Conway, Ernest Yeager, Ralph E. White (eds) *Comprehensive Treatise of Electrochemistry Book Series Vol. 4*, 97–149 (Springer, 1981).
25. Tromans, D. & Sun, R. Anodic polarization behavior of copper in aqueous chloride/benzotriazole solutions. *J. Electrochem. Soc.* **138**, 3235–3244 (1991).
26. Lee, H. P. & Nobe, K. Kinetics and mechanisms of Cu electrodisolution in chloride media. *J. Electrochem. Soc.* **133**, 2035–2043 (1986).
27. Tromans, D. & Silva, J. C. Anodic behavior of copper in iodide solutions: comparison with chloride and effect of benzotriazole-type inhibitors. *J. Electrochem. Soc.* **143**, 458–465 (1996).
28. Barcia, O. E., Mattos, O. R., Peberne, N. & Tribollet, B. Mass-transport study for the electrodisolution of copper in 1M hydrochloric acid solution by impedance. *J. Electrochem. Soc.* **140**, 2825–2832 (1993).
29. Alfantazi, A. M., Ahmed, T. M. & Tromans, D. Corrosion behavior of copper alloys in chloride media. *Mater. Des.* **30**, 2425–2430 (2009).
30. Tait, W. S. Electrochemical corrosion basics, handbook of environmental degradation of materials. In Kutz, M (ed) *Chapter 5 of Handbook of Environmental Degradation of Materials Book* 97–115 (Elsevier Inc., 2018).
31. Perez, N. In *Electrochemistry and Corrosion Science*. 71–120 (Kluwer Academic Publishers Boston, 2016).
32. Lasia, A. In *Electrochemical Impedance Spectroscopy and Its Applications*. 85–125 (Springer, 2014).
33. Brug, G. J., van den Eeden, A. L. G., Sluyters-Rehbach, M. & Sluyters, J. H. The analysis of electrode impedances complicated by the presence of a constant phase element. *J. Electroanal. Chem. Interf. Electrochem* **176**, 275–295 (1984).
34. Hirschorn, B. et al. Determination of effective capacitance and film thickness from constant-phase-element parameters. *Electrochim. Acta* **55**, 6218–6227 (2010).
35. Orzolek, S. M., Semple, J. K. & Fisher, C. R. Influence of processing on the microstructure of nickel aluminum bronze (NAB). *Addit. Manuf.* **56**, 102859 (2022).
36. Culpan, E. A. & Rose, G. Microstructural characterization of cast nickel aluminum bronze. *J. Mater. Sci.* **13**, 1647–1657 (1978).
37. Barbir, F. Fuel cell electrochemistry, PEM fuel cells. In *Chapter 3 of PEM Fuel Cells Book*. 32–72 (Elsevier Inc., 2013).

38. Wei, Y. et al. Effect of annealing temperatures on microstructural evolution and corrosion behavior of Ti-Mo titanium alloy in hydrochloric acid. *Corros. Sci.* **197**, 110079 (2022).
39. Vargel, C. In *Corrosion of Aluminium*. 1–626 (Elsevier, 2004).
40. Wharton, J. A. et al. The corrosion of nickel–aluminium bronze in seawater. *Corros. Sci.* **47**, 3336–3367 (2005).

ACKNOWLEDGEMENTS

The authors express gratitude to the Atlantic Canada Opportunities Agency (ACOA) via the Atlantic Innovation Fund (AIF) under project number 210414 and the Mitacs Accelerate Program through grant number IT10669 for their generous funding that facilitated the execution of this study. The authors also extend their appreciation to Gefertec GmbH in Berlin, Germany, and Alexander Riemann for their contribution to the wire arc additive manufacturing process used to fabricate the nickel–aluminum bronze components. Special acknowledgments are owed to Brian Guidry at UNB–Mechanical Engineering for his assistance in sample machining, and to Dr. Douglas Hall and Steven Cogswell of UNB's Microscopy and Microanalysis facility for their support in SEM and EBSD analysis. The authors would like to thank Prof. Janaki Ram of the Indian Institute of Technology, Hyderabad, for engaging in valuable technical discussions.

AUTHOR CONTRIBUTIONS

A.S. was responsible for devising corrosion experiments, preparing samples, and conducting analyses on corrosion outcomes, as well as examining SEM and TEM findings. A.S. generated the visuals and composed the manuscript. SEM assessments were carried out by D.C., while B.S.A. handled TEM assessments. M.M. and all authors collectively revised the manuscript and engaged in discussions concerning the outcomes and the manuscript itself.

COMPETING INTERESTS

The authors declare no competing interests.

ADDITIONAL INFORMATION

Correspondence and requests for materials should be addressed to Ayda Shahriari.

Reprints and permission information is available at <http://www.nature.com/reprints>

Publisher's note Springer Nature remains neutral with regard to jurisdictional claims in published maps and institutional affiliations.



Open Access This article is licensed under a Creative Commons Attribution 4.0 International License, which permits use, sharing, adaptation, distribution and reproduction in any medium or format, as long as you give appropriate credit to the original author(s) and the source, provide a link to the Creative Commons license, and indicate if changes were made. The images or other third party material in this article are included in the article's Creative Commons license, unless indicated otherwise in a credit line to the material. If material is not included in the article's Creative Commons license and your intended use is not permitted by statutory regulation or exceeds the permitted use, you will need to obtain permission directly from the copyright holder. To view a copy of this license, visit <http://creativecommons.org/licenses/by/4.0/>.

© The Author(s) 2023